A quantitative map of nuclear pore assembly reveals two distinct mechanisms

Shotaro Otsuka[1,3]*, Jeremy O. B. Tempkin[2], Antonio Z. Politi[1,4], Arina Rybina[1], M. Julius Hossain[1], Moritz Kueblbeck[1], Andrea Callegari[1], Birgit Koch[1,5], Andrej Sali[2] and Jan Ellenberg[1]*

[1]Cell Biology and Biophysics Unit, European Molecular Biology Laboratory, Meyerhofstrasse 1, 69117 Heidelberg, Germany.

[2]Department of Bioengineering and Therapeutic Sciences, Department of Pharmaceutical Chemistry, Quantitative Biosciences Institute, University of California, San Francisco, San Francisco, CA 94143, USA.

[3]Present address: Max Perutz Labs, a joint venture of the University of Vienna and the Medical University of Vienna, Vienna Biocenter (VBC), Dr. Bohr Gasse 9, 1030 Vienna, Austria.

[4]Present address: Max Planck Institute for Biophysical Chemistry, Göttingen, Germany.

[5]Present address: Max Planck Institute for Medical Research, Heidelberg, Germany

*Correspondence: shotaro.otsuka@univie.ac.at; jan.ellenberg@embl.de

Summary

Understanding how the nuclear pore complex (NPC) assembles is of fundamental importance to grasp the mechanisms behind its essential function and understand its role during evolution of eukaryotes[1–4]. While we know that at least two NPC assembly pathways exist, one during exit from mitosis and one during nuclear growth in interphase, we currently lack a quantitative map of their molecular events. Here, we use fluorescence correlation spectroscopy (FCS) calibrated live imaging of endogenously fluorescently-tagged nucleoporins to map the changes in composition and stoichiometry of seven major modules of the human NPC during its assembly in single dividing cells. This systematic quantitative map reveals that the two assembly pathways employ

26 strikingly different molecular mechanisms, inverting the order of addition of two large structural
27 components, the central ring complex and nuclear filaments. Our dynamic stoichiometry data
28 allows us to perform the first computational simulation that predicts the structure of postmitotic
29 NPC assembly intermediates.
30
31 The nuclear pore complex (NPC) is the largest non-polymeric protein complex in eukaryotic cells.
32 It spans the double membrane of the nucleus (nuclear envelope; NE) to mediate the
33 macromolecular transport between the nucleus and the cytoplasm. To achieve this essential
34 function, the NPC forms an octameric proteinaceous channel composed of multiples of eight of
35 over 30 different nucleoporins (Nups) that form 6–8 protein modules, the NPC subcomplexes[1,2].
36 Therefore, more than 500 individual proteins have to come together to assemble one nuclear pore,
37 which has the mass of tens of ribosomes. NPCs are thought to represent a key step in the evolution
38 of endomembrane compartmentalization that allowed ancestral eukaryotes to separate their
39 genome from the cytoplasm[3,4].
40 In proliferating cells, there are two main pathways to assemble the NPCs. During nuclear
41 assembly after mitosis, the NPCs form together with nuclear membranes to rapidly build new
42 nuclei in the daughter cells (called postmitotic NPC assembly). During nuclear growth in
43 interphase, NPCs then continue to assemble continuously for homeostasis (referred to as
44 interphase assembly). Research over the last decade has revealed that postmitotic and interphase
45 NPC assembly possess distinct kinetic, molecular and structural features[5–12], suggesting that two
46 fundamentally different mechanisms build the same protein complex. In postmitotic assembly,
47 several thousand NPCs assemble within a few minutes during sealing of the initially fenestrated
48 nuclear membranes, whereas interphase NPC assembly occurs more sporadically, requires about
49 one hour, and involves a new discontinuity in the double membrane barrier of the NE. Studies
50 using molecular depletions have shown that the Nup ELYS is required for postmitotic assembly

51 but appears dispensable for interphase assembly[5], whereas the membrane curvature-sensing
52 domain of Nup133[6], Pom121 and Sun1[7,8], the import of Nup153 into the nucleus[9], and Torsins[10]
53 seem to be required only for interphase assembly. Recent studies correlating real time imaging
54 with three-dimensional electron microscopy have revealed that postmitotic NPC assembly
55 proceeds by radial dilation of small membrane openings[11], while in interphase, assembly induces
56 an asymmetric inside-out fusion of the inner and outer nuclear membranes[12].

57 However, how several hundred proteins self-organize to form the NPC channel *via* these two
58 distinct assembly pathways has remained largely enigmatic. It is technically challenging to locate
59 the transient and rare assembly events, which has prevented investigation of the structure of
60 assembly intermediates by either cryo-EM tomography or super-resolution microscopy. In
61 addition, the large number of building blocks and their cooperativity often leads to complex
62 nonlinear kinetics that can only be interpreted mechanistically using computational modelling of
63 the structures formed during assembly. While we have some information about the dynamic
64 addition of Nups after mitosis[13,14], only sparse dynamic data is available for interphase
65 assembly[15,16]. Importantly, these earlier studies could not distinguish postmitotic and interphase
66 assemblies, whose co-occurrence in different regions of the nucleus was only discovered later;
67 moreover, these studies provided only qualitative descriptions as they relied on ectopic expression
68 of fluorescently-tagged Nups. Kinetic data about NPC assembly that can distinguish between the
69 postmitotic and interphase pathways is required, including the copy numbers of Nups that
70 assemble into forming NPCs over time. Such data would enable modeling of the assembly process
71 and allow us to start to understand the two assembly mechanisms.

72

73 **Quantitative live imaging of ten nucleoporins representing seven major NPC building blocks**

74 To quantitatively analyze the changes in concentration of Nups at the NE during exit from mitosis
75 and nuclear growth in G1, we genome-edited HeLa cells, homozygously tagging the endogenous

76 genes for ten different Nups with mEGFP or mCherry. We chose proteins that represent the major
77 building blocks of the fully assembled pore, including the nuclear filament protein Tpr, the nuclear
78 Nup153, the Y-complex members Nup107 and Seh1, the central ring complex members Nup93
79 and Nup205, the central channel protein Nup62, the transmembrane protein Pom121 as well as the
80 cytoplasmic filament proteins Nup214 and Nup358. Homozygous tagging was verified by careful
81 quality control of the genome edited monoclonal cell lines[17], ensuring that the tagged subunit was
82 expressed at physiological levels, localized to the NPC and that cell viability and mitotic
83 progression were normal (Figs. 1 and 2). The fusion proteins are likely functional, given that most
84 Nups show strong phenotypes upon knock-out or depletion[18].

85 To characterize the fluorescently-tagged Nups, we first performed super-resolution (STED)
86 microscopy to determine NPC density in fully grown nuclei of the knock-in cell lines, showing
87 that homozygous tagging had little effect on NPC density that was comparable within 15%
88 between all cell lines with an average of 10.1 NPC per μm^2 (Fig. 1b, c), in good agreement with
89 our previous estimates by electron microscopy of HeLa cells[12]. We then used fluorescence
90 correlation spectroscopy (FCS) calibrated confocal microscopy[19,20] to determine the concentration
91 and total number of the Nups at the NE in living cells (Extended Data Table 1, for details see
92 Methods). Using the measured NPC density and the Nup concentration at the NE, we could
93 calculate the average copy number of each Nup per NPC (Fig. 1d). This data showed that the
94 investigated Nups were on average present in 16, 32, or 48 copies per pore, as expected from the
95 eightfold symmetry of the complex and overall in good agreement with previous estimates by mass
96 spectrometry[21]. This observation quantitatively validated that the homozygous tagging did not
97 affect the incorporation of the Nups into the NPC. For Nup153 and Pom121 that exhibited lower
98 concentrations likely due to subhomozygous tagging (Fig. 2a, Extended Data Fig. 1), we
99 normalized their stoichiometry to the expected number of copies in the mature pore for comparison
100 (Fig. 3a).

101

102 **NPC assembly relies on and consumes almost half of the material inherited from the mother**
103 **cell within one hour after mitosis**

104 We then used our validated cell line resource to quantitatively image the Nups during both
105 postmitotic and interphase NPC assembly, from metaphase until the end of the rapid nuclear
106 growth phase in G1, two hours after anaphase onset. To this end, we performed systematic FCS-
107 calibrated 3D confocal time-lapse microscopy[22] (Fig. 2a). Using the single molecule fluctuation
108 calibration, the 4D imaging data could be converted into maps of subcellular protein concentration
109 (Fig. 2a). Counterstaining live nuclei with SiR-DNA[23], enabled computational image
110 segmentation to measure the soluble cytoplasmic pool and the NE associated pool over time[22].
111 Temporal alignment to anaphase onset then allowed us to compare the dynamic association of all
112 Nups with the NE over time (Fig. 2a). Overall, the investigated Nups are present in 250,000 to
113 1,200,000 copies per human metaphase cell. After mitosis, this building material is split between
114 the daughter cells with little detectable new protein synthesis in the first hour after anaphase onset
115 (Fig. 2b). Notably, 34–53% of the soluble pool present in the cytoplasm in metaphase was rapidly
116 re-localized to the NE during the first hour after exit from mitosis (43, 38, 47, 37, 41, 44, 53, and
117 34% for Nup107, Seh1, Nups205, 93, 62, 214, Tpr and Nup358, respectively) (Fig. 2b), indicating
118 that NPC assembly initially relies almost entirely on the pool of building blocks inherited from the
119 mother cell to form the first 4,000–5,000 NPCs[11,12].

120

121 **Quantitative analysis of multimolecular kinetics of postmitotic and interphase NPC**
122 **assembly**

123 As we and others have demonstrated previously[12,24], postmitotic and interphase NPC assembly can
124 be observed in the same living cell in different regions of the NE within the first two hours after
125 mitosis. While postmitotic assembly dominates the peripheral “non-core” regions of the NE, the

126 central "inner core" area is only populated with NPCs after exit from mitosis when dense spindle
127 microtubules have been removed from the DNA surface[25]. Using computational segmentation and
128 assignment of the inner-core and non-core regions (Extended Data Fig. 2a), we measured the
129 concentration changes of the ten Nups in these two regions separately. A two-component model
130 of a fast (postmitotic) and a slow (interphase) assembly process fits the experimental data well,
131 allowing us to kinetically unmix the two assembly processes for each Nup (Extended Data Figs.
132 2b–d and 3). In this way, we could for the first time perform an integrated analysis of the real time
133 kinetics of absolute concentration changes of Nups in all major NPC modules during the two
134 assembly processes at the NE (Fig. 3a). This analysis immediately revealed that the overall
135 duration of the two processes is very different, with postmitotic assembly essentially complete 15
136 min after anaphase onset, while interphase assembly only reaches a plateau after 100 min,
137 consistent with our previous estimates based on live cell imaging[13,16] and correlative electron
138 microscopy[11,12]. Both processes reached the same final ratios between the different Nups and thus
139 presumably formed identical NPCs. However, the temporal order in which components were
140 added was distinct, including, for example, an earlier assembly of Pom121 relative to the Y-shaped
141 complex during interphase assembly, consistent with our previous observations[16].

142 To comprehensively investigate the molecular differences between the two assembly
143 processes, we relied on the constant NPC density and changes in nuclear surface area[12] to convert
144 the NE concentrations of all investigated Nups into their average copy number per assembling
145 NPC over time (Fig. 3a). This result in turn enabled us to estimate changes in subunit stoichiometry
146 of the complex during its assembly in living cells. To facilitate the comparative analysis of the
147 assembly kinetics between the two pathways, in which ten components assemble with different
148 speed and order, we first reduced the dimensionality of the kinetic data. To this end, we assigned
149 a single characteristic time-point of assembly to each Nup, by sigmoidal fitting of its full kinetic
150 signature (Extended Data Fig. 4a). Plotting the copy number *vs* the average time-point of assembly

151 provides an overview of the major molecular differences between the two assembly pathways (Fig.
152 3b).

153 While the Y-complex, Pom121, and Nup153 form a core of the first modules that assemble
154 almost simultaneously within one minute in postmitotic assembly, these components are stretched
155 out into a clear temporal order of first Nup153, second Pom121, and third the Y-complex (notably
156 with its two investigated subunits also assembling simultaneously in interphase) over more than
157 ten minutes in interphase assembly. The end of assembly on the other hand is marked for both
158 process by the addition of the large cytoplasmic filament protein Nup358. The major difference
159 was thus neither in initiation nor termination of assembly, but rather in the middle of the two
160 assembly pathways. During postmitotic assembly, the Y-complex is rapidly combined with
161 components of the central ring, building the inner core of the pore within only three minutes prior
162 to addition of either cytoplasmic or nuclear filament proteins, which follow later. In contrast,
163 during interphase assembly, the Y-complex is first combined with the nuclear filament protein Tpr
164 and the base of the cytoplasmic filament Nup214, while the central ring complex is added later.
165 This observation clearly shows that postmitotic and interphase NPC assembly not only proceed
166 with different speed but also follow a different molecular mechanism using an inverted molecular
167 order between the central ring and nuclear filaments (Fig. 3b, Extended Data Fig. 4b).

168 To obtain additional insight into the assembly mechanism, it is instructive to go beyond
169 examining the temporal order and examine our data for evidence of coupling between different
170 components of the NPC. Theoretically, for a sequential assembly mechanism where late steps
171 depend on early steps, the observed ensemble kinetics of a late binding protein must contain the
172 history of all previous events (see Methods for details). To test this prediction, we examined if one
173 or both of our assembly pathways exhibited a correlation between the average assembly time and
174 duration of the different components. We plotted the time needed for 90% of one protein to
175 accumulate in the population of assembling pores (the assembly duration) *vs* the time when this

176 accumulation is half maximal in the overall process (the average time-point of assembly) for all
177 analysed Nups (Fig. 3c, Extended Data Fig. 4a). Indeed, postmitotic assembly showed a strong
178 positive linear correlation (Fig. 3c), indicating a sequential assembly mechanism, which for
179 example implies that Nup62 is incorporated into the NPC before Tpr can bind. In contrast,
180 interphase assembly shows poor correlation between duration and time-point of assembly (Fig.
181 3c), indicating a less strictly sequential pathway, where proteins may assemble more
182 independently of each other.
183
184 **Integrative modeling of the NPC assembly pathway**
185 To obtain a more comprehensive mechanistic view, we computed a spatiotemporal model of the
186 macromolecular assembly pathway, based on our dynamic multimolecular stoichiometry data in
187 combination with the available ultrastructural data about NPC assembly[11] and the partial
188 pseudoatomic model of the mature NPC[26,27]. We modeled here only the postmitotic assembly, as
189 it showed the kinetic hallmarks of a sequential process and is known to proceed by dilating an
190 existing membrane pore with a smoothly growing proteinaceous density[11]. We focused on the
191 Nups contained in the structural model of the human NPC, including Nup107 and Seh1 for the Y-
192 complex as well as Nup93, Nup205, and Nup62 for the central ring/channel complex[26,27]. We
193 constrained their copy number by our stoichiometry data for the time points for which correlative
194 electron tomography data is available[11], in order to use the membrane shapes and associated
195 protein densities from the tomography to constrain Nup positions. To structurally model the
196 spatiotemporal assembly process, we generalized our integrative modeling method for determining
197 static structures of macromolecular assemblies[28,29]. In outline (see Methods for details), we first
198 model ensembles of structures at discrete time points, then connect them between time points into
199 assembly trajectories and finally rank the alternative trajectories by fit to our data.

200 We focus on the best fitting macromolecular assembly pathway that accounts for over 80% of
201 the posterior model density (the second-scoring accounts for only 19%). This trajectory starts by
202 formation of a single nuclear ring, composed of eight Y-complexes, concomitantly with an initial
203 accumulation of the FG-repeat protein Nup62 and Nup205 in the center of the membrane hole
204 (Fig. 4). The cytoplasmic Y-complex is then added on the cytoplasmic side, before the second set
205 of the Y-complex ring assembles on the nuclear side, again one eight-membered ring after another.
206 In the center of the pore, Nup62 dilates from an amorphous mass into a small ring and associates
207 with Nup205 to form the central ring complex. This "nuclear ring first" assembly mechanism is
208 consistent with the observation of an eight-fold symmetric protein density on the inner nuclear
209 membrane at early stages of assembly[11]. In addition, the early accumulation of Nup62 to the pore
210 center suggests a potential role of the hydrophobic FG-repeats in the initial dilation of the small
211 membrane hole into the larger, NPC sized channel.
212
213 **Discussion**
214 Our data revealed that the two assembly pathways employ strikingly different molecular
215 mechanisms. While it is at first glance surprising that the cell builds the same machine in two
216 fundamentally different ways, these distinct pathways can be rationalized by considering them in
217 the light of the rather different physiological requirements that the cell faces after mitosis and
218 during nuclear growth in interphase. Immediately after exit from mitosis, the nucleus is formed *de*
219 *novo* and the cell needs to rapidly seal its genome, exclude cytoplasm from it[30] and quickly restore
220 import of essential nuclear proteins. Since the new NE originates from highly fenestrated ER
221 sheets, nuclear transport channels can be built without a formal membrane fusion requirement[11].
222 The mechanism we observed for postmitotic assembly, appears well adapted to this context. The
223 rapid assembly of the nuclear Y-ring and the central ring could provide a fast way to prevent
224 complete fusion of the ER membrane holes and assemble a minimal, transport competent

225 proteinaceous phase in them. Assembly of this first "transport core" NPC is complete within less
226 than 10 min after mitosis, which precisely matches the time when transport competence is gained
227 by postmitotic nuclei[13,14].

228 By contrast in telo/G1 phase, the nucleus already has a sealed, double membraned NE with
229 about 2500 postmitotically assembled and transporting pores, but needs to expand to allow the
230 genome to take up its interphase functions. To support nuclear growth, the cell needs to maintain
231 a constant NPC density to ensure sufficient transport capacity and maintain homeostasis to provide
232 enough NPC building blocks for the next cell generation, which we have shown to initially rely
233 completely on material from the mother cell. Interphase NPC assembly requires a *de novo* fusion
234 between the inner and outer nuclear membrane but must not disrupt nuclear integrity. The
235 molecular pathway we observed for interphase assembly makes new predictions about its unique,
236 inside out evaginating, mechanism. The cell first not only builds the two nuclear Y-rings but also
237 accumulates the material for their cytoplasmic counterparts and then combines them with the
238 nuclear filament proteins, all prior to the time of membrane fusion[12]. This mechanism suggests
239 that the cytoplasmic Y-rings, including the base of the cytoplasmic filaments with Nup214, are
240 already "prebuilt" within the inner membrane evagination, where the small available volume
241 would predict that they must be present in a very different structure than in the fully mature pore
242 after fusion. In addition, the unexpectedly early presence of Tpr suggests a key role of this large
243 coiled-coil protein during interphase assembly, potentially in the membrane bending and/or fusion
244 process. Surprisingly, the central ring complex, which is a core structural element between the
245 nuclear and cytoplasmic Y-rings in the mature pore[27] is added only later, suggesting that during
246 interphase assembly, nuclear transport control may only be added after the membrane fusion step.
247 The order of Nup assembly for interphase assembly we observed here is consistent with the
248 recently reported order of NPC assembly in budding yeast that undergoes a closed mitosis[31], except
249 for the Tpr homologues Mlp1/2 which assemble late in yeast[31]. This difference could be due to the

250 fundamental differences in cell cycle remodeling of the NE or additional functions of Mlp proteins
251 that are believed to compensate for the absence of lamins in yeast.

252 Beyond the assembly mechanism the two pathways we have mapped here start to shed light
253 on the role of the NPC during evolution of the endomembrane system in eukaryotes[3,4]. We
254 speculate that the modern NPC combines ancient membrane bending (e.g. coiled-coil filaments,
255 such as Tpr) and membrane hole plugging (e.g. FG-repeat proteins of the central ring complex)
256 modules, that were potentially previously used separately for extruding the cell surface or keeping
257 transport channels open in the endomembranes around the genome. The key evolutionary
258 innovation might lie in combining and controlling these activities, potentially by the eight-
259 membered ring architecture of the nuclear Y-complex. In the future, comparing NPC assembly
260 pathways in different species on the eukaryotic evolutionary tree, might help us to understand how
261 the assembly of complex modern protein machines reflects their evolutionary origins.

262

263 **Main references**

264 1 Hampoelz, B., Andres-Pons, A., Kastritis, P. & Beck, M. Structure and Assembly of the
265 Nuclear Pore Complex. *Annu. Rev. Biophys.* **48**, 515–536 (2019).

266 2 Lin, D. H. & Hoelz, A. The Structure of the Nuclear Pore Complex (An Update). *Annu.*
267 *Rev. Biochem.* **88**, 725–783 (2019).

268 3 Baum, D. A. & Baum, B. An inside-out origin for the eukaryotic cell. *BMC Biol.* **12**, 76
269 (2014).

270 4 Otsuka, S. & Ellenberg, J. Mechanisms of nuclear pore complex assembly - two different
271 ways of building one molecular machine. *FEBS lett.* **592**, 475–488 (2018).

272 5 Franz, C. *et al.* MEL-28/ELYS is required for the recruitment of nucleoporins to chromatin
273 and postmitotic nuclear pore complex assembly. *EMBO Rep.* **8**, 165–172 (2007).

274 6 Doucet, C. M., Talamas, J. A. & Hetzer, M. W. Cell cycle-dependent differences in nuclear
275 pore complex assembly in metazoa. *Cell* **141**, 1030–1041 (2010).
276 7 Talamas, J. A. & Hetzer, M. W. POM121 and Sun1 play a role in early steps of interphase
277 NPC assembly. *J. Cell Biol.* **194**, 27–37 (2011).
278 8 Funakoshi, T., Clever, M., Watanabe, A. & Imamoto, N. Localization of Pom121 to the
279 inner nuclear membrane is required for an early step of interphase nuclear pore complex
280 assembly. *Mol. Biol. Cell* **22**, 1058–1069 (2011).
281 9 Vollmer, B. *et al.* Nup153 Recruits the Nup107-160 Complex to the Inner Nuclear
282 Membrane for Interphasic Nuclear Pore Complex Assembly. *Dev. Cell* **33**, 717-728 (2015).
283 10 Rampello, A. J. *et al.* Torsin ATPase deficiency leads to defects in nuclear pore biogenesis
284 and sequestration of MLF2. *J. Cell Biol.* **219** (2020).
285 11 Otsuka, S. *et al.* Postmitotic nuclear pore assembly proceeds by radial dilation of small
286 membrane openings. *Nat. Struct. Mol. Biol.* **25**, 21–28 (2018).
287 12 Otsuka, S. *et al.* Nuclear pore assembly proceeds by an inside-out extrusion of the nuclear
288 envelope. *Elife* **5** (2016).
289 13 Dultz, E. *et al.* Systematic kinetic analysis of mitotic dis- and reassembly of the nuclear
290 pore in living cells. *J. Cell Biol.* **180**, 857–865 (2008).
291 14 Otsuka, S., Szymborska, A. & Ellenberg, J. Imaging the assembly, structure, and function
292 of the nuclear pore inside cells. *Methods Cell Biol.* **122**, 219–238 (2014).
293 15 D'Angelo, M. A., Anderson, D. J., Richard, E. & Hetzer, M. W. Nuclear pores form de
294 novo from both sides of the nuclear envelope. *Science* **312**, 440–443 (2006).
295 16 Dultz, E. & Ellenberg, J. Live imaging of single nuclear pores reveals unique assembly
296 kinetics and mechanism in interphase. *J. Cell Biol.* **191**, 15–22 (2010).
297 17 Koch, B. *et al.* Generation and validation of homozygous fluorescent knock-in cells using
298 CRISPR-Cas9 genome editing. *Nat. Protoc.* **13**, 1465–1487 (2018).

299 18 Guglielmi, V., Sakuma, S. & D'Angelo, M. A. Nuclear pore complexes in development
300 and tissue homeostasis. *Development* **147** (2020).
301 19 Wachsmuth, M. *et al.* High-throughput fluorescence correlation spectroscopy enables
302 analysis of proteome dynamics in living cells. *Nat. Biotechnol.* **33**, 384–389 (2015).
303 20 Politi, A. Z. *et al.* Quantitative mapping of fluorescently tagged cellular proteins using
304 FCS-calibrated four-dimensional imaging. *Nat. Protoc.* **13**, 1445–1464 (2018).
305 21 Ori, A. *et al.* Cell type-specific nuclear pores: a case in point for context-dependent
306 stoichiometry of molecular machines. *Mol. Syst. Biol.* **9**, 648 (2013).
307 22 Cai, Y. *et al.* Experimental and computational framework for a dynamic protein atlas of
308 human cell division. *Nature* **561**, 411–415 (2018).
309 23 Lukinavicius, G. *et al.* SiR-Hoechst is a far-red DNA stain for live-cell nanoscopy. *Nat.*
310 *Commun.* **6**, 8497 (2015).
311 24 Maeshima, K. *et al.* Cell-cycle-dependent dynamics of nuclear pores: pore-free islands and
312 lamins. *J. Cell Sci.* **119**, 4442–4451 (2006).
313 25 Vietri, M. *et al.* Spastin and ESCRT-III coordinate mitotic spindle disassembly and nuclear
314 envelope sealing. *Nature* **522**, 231–235 (2015).
315 26 von Appen, A. *et al.* In situ structural analysis of the human nuclear pore complex. *Nature*
316 **526**, 140–143 (2015).
317 27 Kosinski, J. *et al.* Molecular architecture of the inner ring scaffold of the human nuclear
318 pore complex. *Science* **352**, 363–365 (2016).
319 28 Kim, S. J. *et al.* Integrative structure and functional anatomy of a nuclear pore complex.
320 *Nature* **555**, 475–482 (2018).
321 29 Rout, M. P. & Sali, A. Principles for Integrative Structural Biology Studies. *Cell* **177**,
322 1384–1403 (2019).

30 Cuylen-Haering, S. *et al.* Chromosome clustering by Ki-67 excludes cytoplasm during nuclear assembly. *Nature*, **587**, 285–290 (2020).

31 Onischenko, E. *et al.* Maturation Kinetics of a Multiprotein Complex Revealed by Metabolic Labeling. *Cell* **183**, 1785–1800 (2020).

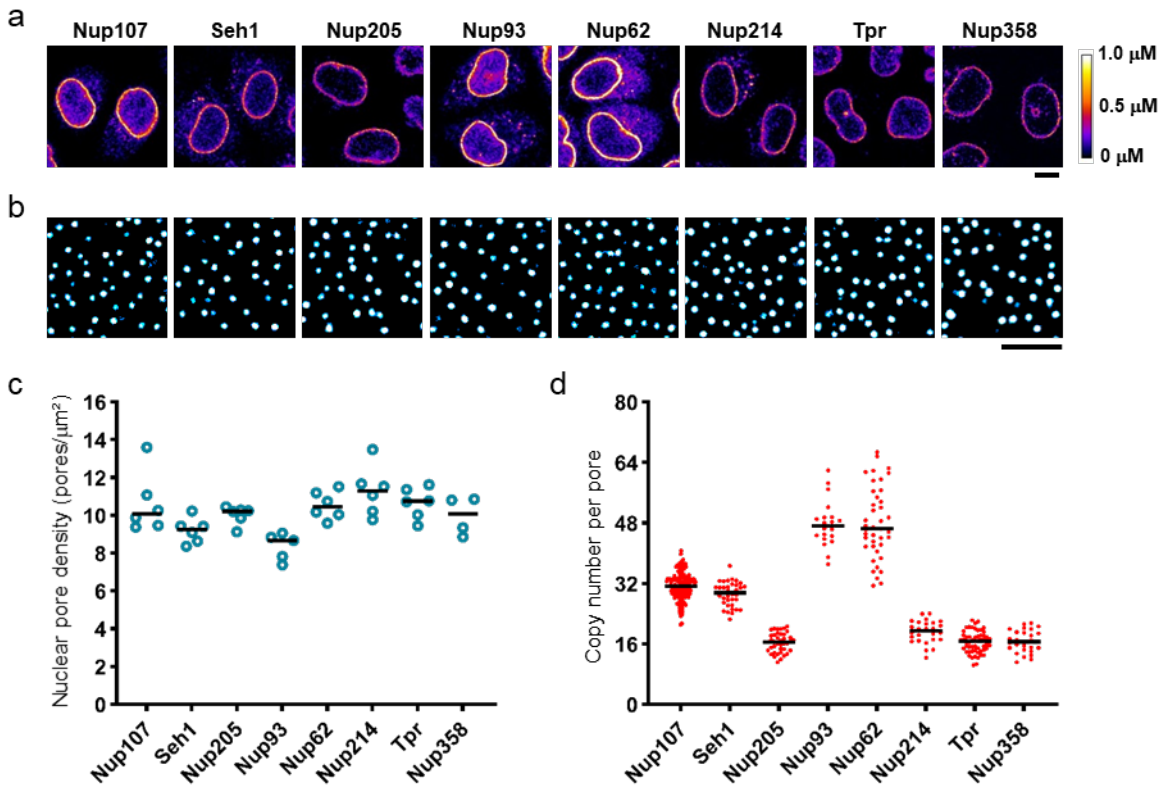

Fig. 1 | Quantitative imaging of GFP-knock-in nucleoporin (Nup) cell lines. **a**, Genome-edited HeLa cells with homozygously mEGFP-tagged Nups observed by confocal microscopy. Fluorescent intensity was converted into protein concentration by FCS-calibrated imaging[20]. Images were filtered with a median filter (kernel size: 0.25 × 0.25 μm) for presentation purposes. Scale bar, 10 μm. **b**, **c**, Stimulated emission depletion (STED) microscopy. The genome-edited cells were stained with anti-Nup62 antibody and imaged (**b**), and then the density of nuclear pores was quantified (**c**). The plot is from 6, 6, 6, 5, 6, 6, 6, and 4 cells for Nup107, Seh1, Nup205, Nup93, Nup62, Nup214, Tpr and Nup358, respectively. Scale bar, 1 μm. **d**, Calculated copy number of Nups per nuclear pore. The plot is from 241, 37, 41, 20, 41, 26, 55, and 28 cells for Nup107, Seh1, Nup205, Nup93, Nup62, Nup214, Tpr and Nup358, respectively. The median is depicted as a line.

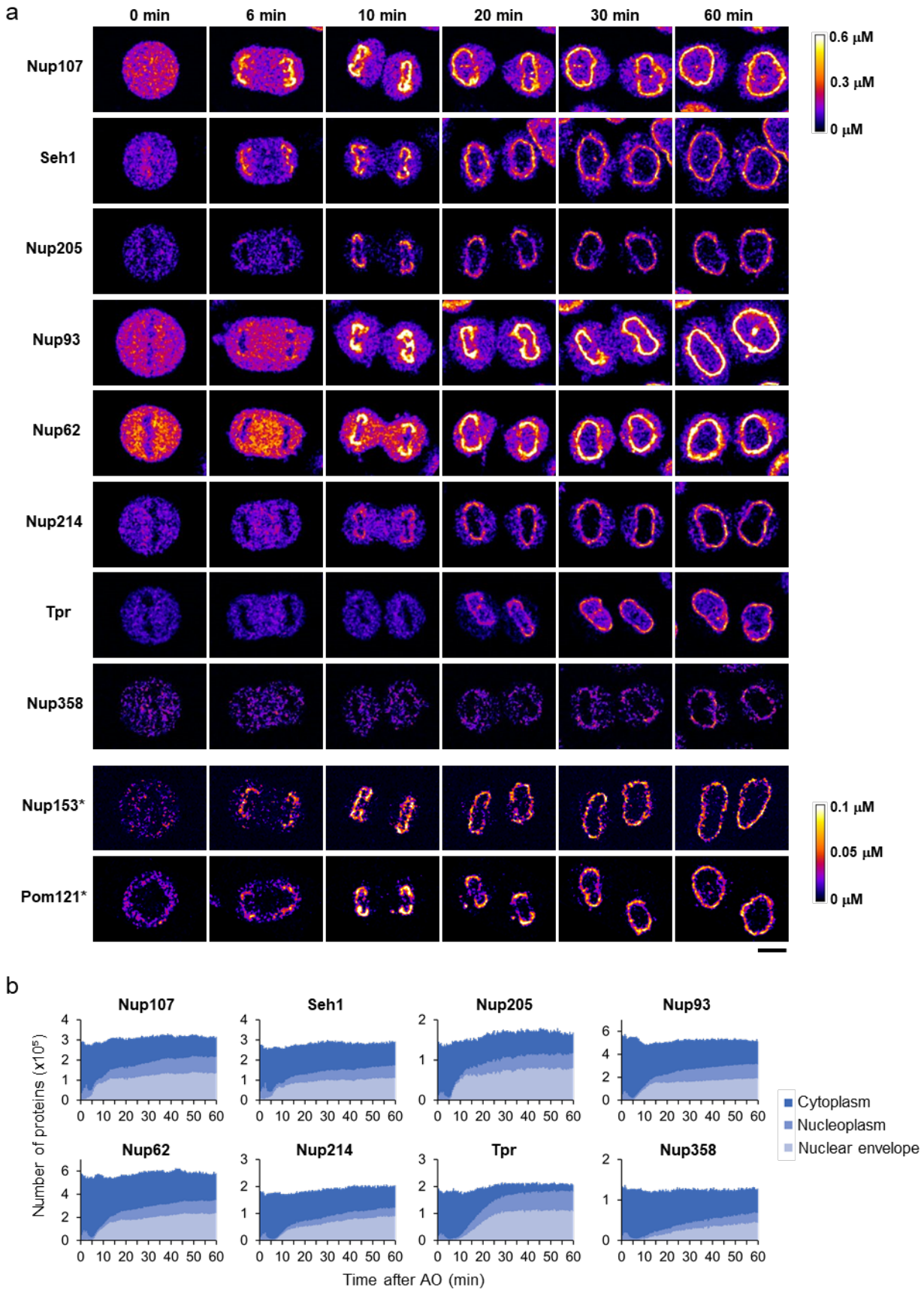
a
0 min
6 min
10 min
20 min
30 min
60 min
Nup107
Seh1
Nup205
Nup93
Nup62
Nup214
Tpr
Nup358
Nup153*
Pom121*
0.6 µM
0.3 µM
0 µM
0.1 µM
0.05 µM
0 µM
b
Nup107
Seh1
Nup205
Nup93
Nup62
Nup214
Tpr
Nup358
Number of proteins (x10⁵)
Time after AO (min)
Cytoplasm
Nucleoplasm
Nuclear envelope

339
340

Fig. 2 | Dynamic concentration maps of Nups after anaphase onset (AO).
a, HeLa cells whose Nups are endogenously tagged with mEGFP or mCherry were imaged every 30 sec by three-dimensional confocal microscopy. Single confocal sections are shown. Images were calibrated by FCS to convert fluorescence intensities into cellular protein concentration. *For Nup153 and Pom121, these Nups are not fully validated to be homozygously-tagged. Images were filtered with a median filter (kernel size: 0.25 × 0.25 μm). Scale bar, 10 μm. **b**, Dynamic change of Nup numbers during mitotic exit. The number of Nups in cytoplasm (dark blue), nucleoplasm (medium dark blue) and nuclear envelope (light blue) are plotted against time after anaphase onset. The plot is the mean of 15, 20, 13, 14, 22, 22, 19, and 24 cells for Nup107, Seh1, Nup205, Nup93, Nup62, Nup214, Tpr and Nup358, respectively.

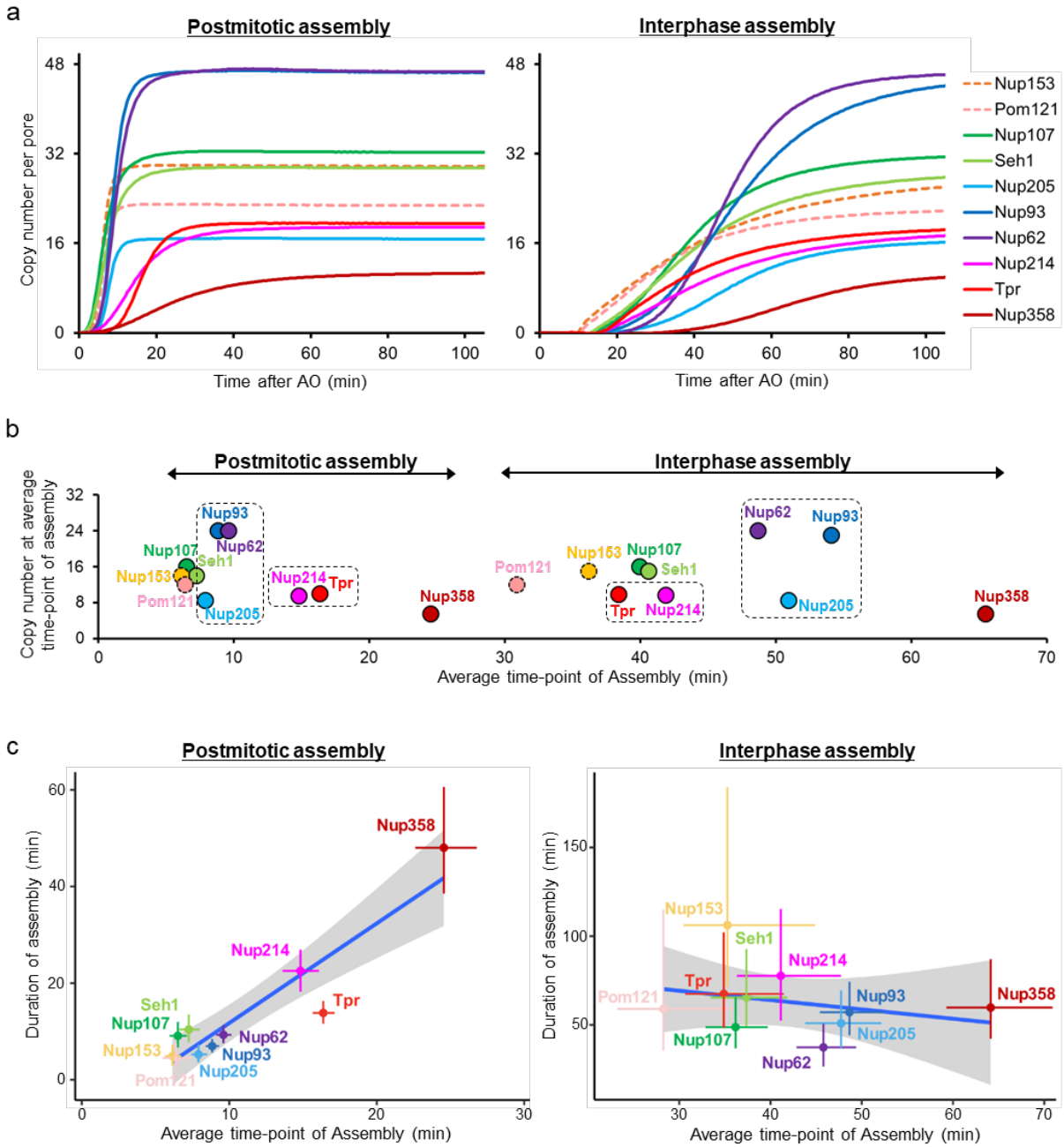

Fig. 3 | The molecular assembly order and maturation kinetics are distinct for postmitotic and interphase assembly.

a, Plots of the average copy number per nuclear pore computed from mathematical modeling for postmitotic (left) and interphase (right) assembly (see Methods and Extended Data Figs. 2 and 3 for details). For Nup153 and Pom121 (dashed lines), their absolute amount was estimated using the copy number determined from the previous study (32 for Nup153 and 16 for Pom121)[21]. **b**, The average copy number of individual Nups per nuclear pore are plotted along their average time-points of assembly in postmitotic and interphase assembly pathways. **c**, Plots of Nup assembly duration along the time-point of assembly for postmitotic and interphase assembly pathways. The crosses indicate the 95% confidence intervals. The dots are the mean values. Values are listed in Extended Data Table 2. The long straight line shows the result of a linear regression to the mean values. The gray area is the 95% confidence interval of the linear regression.

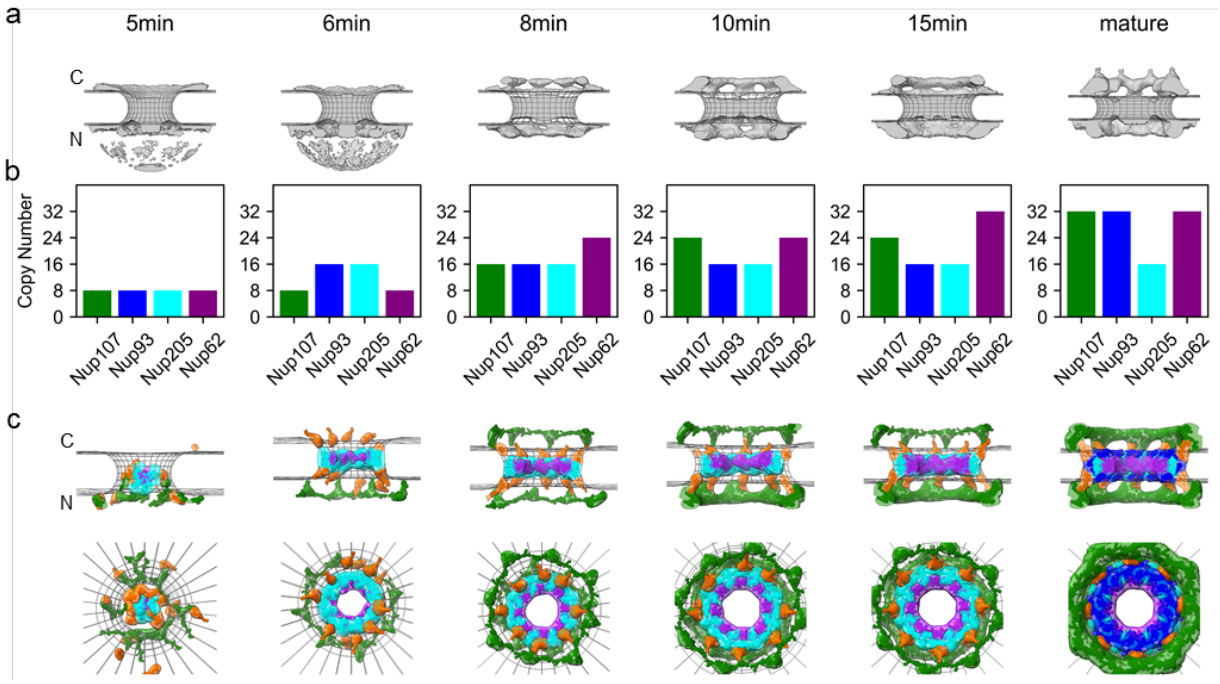

365
366 **Fig. 4 | Integrative model of the postmitotic NPC assembly pathway**.
367 **a**, Protein density (grey) overlaid with the NE surface (wireframe model, grey) at each time
368 point. C, cytoplasm; N, nucleoplasm. **b**, Copy numbers of Nups used to construct a static NPC
369 model at each time point. **c**, The best-scoring model of postmitotic assembly pathway (top and
370 side views). The uncertainty of each Nup localization is indicated by the density of the
371 corresponding color: Y-complex (green), Nup93-Nup188-Nup155 complex (blue), Nup205-
372 Nup93-Nup155 complex (cyan), Nup62-Nup54 complex (purple), and Nup155 (orange).

373 **Methods**

374 **Cell culture**

375 Wildtype HeLa kyoto cells (RRID: CVCL_1922) were kind gift from Prof. Narumiya in Kyoto
376 University, and the genome was sequenced previously[32]. Cells were grown in high glucose
377 Dulbecco's Modified Eagle's Medium (DMEM) containing 4.5 g/l D-glucose (Sigma Aldrich, St.
378 Louis, MO) supplemented with 10% fetal calf serum (FCS), 2 mM l-glutamine, 1 mM sodium
379 pyruvate, and 100 μg/ml penicillin and streptomycin at 37 °C and 5% CO_2. The mycoplasma
380 contamination was inspected by PCR every 2 or 3 months and was always negative.

381

382 **Genome editing**

383 Monomeric enhanced GFP (mEGFP) and mCherry were inserted into the genome using zinc finger
384 nucleases or CRISPR-Cas9 nickases[17]. The following six cell lines had been generated and
385 published previously: Nup62-mEGFP[33], mEGFP-Nup107[12], mEGFP-Nup205[11], mEGFP-Nup214,
386 mEGFP-Nup358 (also called RanBP2) and Tpr-mEGFP[22]. The following four cell lines were
387 generated in this study: mEGFP-Seh1, Nup93-mEGFP, mEGFP-Nup153, and Pom121-mCherry.
388 The gRNA sequences used for generating these cell lines are summarized in Extended Data Table
389 3. For the Nup93-mEGFP cell line, CRISPR-Cas9 nickases and the donor plasmid were transfected
390 by electroporation (Neon Transfection System, Thermo Fisher Scientific, Waltham, MA) instead
391 of a polymer-mediated transfection reagent.

392

393 **FCS-calibrated live-cell imaging and estimation of Nup copy numbers per NPC**

394 (i) Wild-type cells, (ii) wild-type cells transfected with mEGFP using Fugene6 (Promega,
395 Madison, WI), (iii) mEGFP-Nup107 genome-edited cells, and (iv) the cells of another mEGFP-
396 Nup genome-edited cell line, were seeded on each well of 8-well Lab-Tek Chambered Coverglass
397 (Thermo Fisher Scientific). On the day of live-cell imaging, DMEM was replaced by imaging

398 medium: CO_2-independent medium without phenol red (Invitrogen) containing 20% FCS, 2 mM
399 l-glutamine, and 100 μg/ml penicillin and streptomycin. The imaging medium was supplemented
400 with 50 nM silicon–rhodamine (SiR) Hoechst[23]. Cells were incubated inside the microscope-body-
401 enclosing incubator at 37 °C for at least 30 min before imaging.

402 Calibrated imaging using fluorescence correlation spectroscopy (FCS) was carried out as
403 described in a previous report[20]. Briefly, the confocal volume was determined by performing FCS
404 using a dye with known diffusion coefficient and concentration (Alexa Fluor 488 NHS ester;
405 Thermo Fisher Scientific for mEGFP, Alexa Fluor 568 NHS ester; Thermo Fisher Scientific for
406 mCherry). To convert fluorescence intensity to the concentration, FCS was performed in the cells
407 that transiently-express mEGFP or mCherry alone. Then a calibration curve was obtained by
408 plotting the fluorescence intensity along the concentration. The background fluorescence signal
409 was measured in cells without expressing fluorescent proteins and subtracted.

410 To measure the concentration of Nups, mEGFP-Nup genome-edited cells in interphase were
411 imaged in 3D using a confocal microscope (LSM780; Carl Zeiss, Oberkochen, Germany) and a
412 40× 1.2 NA C-Apochromat water immersion objective (Carl Zeiss) at 37 °C in a microscope-body-
413 enclosing incubator, under the following conditions: 21 optical sections, section thickness of 2.0
414 μm, z-stacks of every 1.0 μm, and the xy pixel size of 0.25 μm. When the NE is not perpendicular
415 to the confocal plane of the 3D stacks, the fluorescence intensity at the NE is nonisotropic in the
416 point-spread function (PSF), which results in underestimation of the signal. To avoid such
417 underestimation, a single plane was selected that contains the largest nuclear area in which the NE
418 is perpendicular to the imaging plane and thus isotropic in the PSF. The fluorescence intensity of
419 Nups was quantified on this single plane using the NE mask with the width of three pixels (0.75
420 μm) that was generated from a SiR-DNA channel. Background fluorescence intensity was
421 measured in wild-type cells without expressing any fluorescent proteins and subtracted. The Nup
422 fluorescence intensity on the NE was converted to the concentration using the calibration curve

423 generated by FCS above. The number of Nups per square micro-meter was calculated from the
424 concentration and then divided by the NPC density per square micro-meter measured by stimulated
425 emission depletion (STED) microscopy. This absolute quantification of Nup copy number with
426 FCS calibration was done using 47 mEGFP-Nup107 genome-edited cells in interphase. For other
427 mEGFP-Nups genome-edited cells, their Nup fluorescent intensities on the NE were directly
428 compared with the ones of mEGFP-Nup107 genome-edited cells on the same 8-well Lab-Tek
429 Chambered Coverglass, and then their concentrations were determined using the intensity ratios
430 to the mean intensity of mEGFP-Nup107 without using a FCS calibration curve. For Pom121-
431 mCherry, the copy number was quantified independently.
432
433 **Measurement of nuclear pore density by stimulated emission depletion (STED) microscopy**
434 For STED super-resolution imaging, cells were fixed with 2.4% formaldehyde (Electron
435 Microscopy Sciences, Hatfield, PA) in PBS for 10 min, extracted with 0.4% Triton X-100 (Sigma
436 Aldrich) in PBS for 5 min, and blocked with 5% normal goat serum (Life Technologies, Carlsbad,
437 CA) in PBS for 10 min at room temperature. Subsequently, the cells were incubated overnight at
438 4°C with a mouse anti-Nup62 (Cat. No. 610497; BD Biosciences, Franklin Lakes, NJ) antibody,
439 and then with an Abberior® STAR RED-conjugated anti-mouse IgG (Cat. No. 2-0002-011-2,
440 Abberior GmbH, Göttingen, Germany) for 30 min at room temperature. After multiple washes in
441 PBS, cells were mounted in Vectashield (Cat. No. H-1500, Vector Laboratories Inc., Burlingame,
442 CA). Super-resolution imaging was performed on a Leica SP8 3X STED microscope as described
443 in a previous report[12]. The images were taken with a final optical pixel size of 20 nm, z-stacks of
444 every 250 nm, and the optical section thickness of 550 nm. Images were filtered with a Gaussian
445 filter (kernel size: 0.5 × 0.5 pixel) for presentation purposes. The shrinkage of the nucleus by
446 formaldehyde fixation was quantified by comparing the volume of the nuclei of live cells with the
447 ones of fixed cells. The shrinkage was 9.1 ± 2.6% (the average and standard error, N = 36 cells).

448 The NPC density was corrected for the nuclear shrinkage for the calculation of Nup copy number
449 per NPC in Fig. 1d.
450 To quantify NPC density, the raw STED data were processed in ImageJ
451 (http://rsbweb.nih.gov/ij/) with a mean filter (kernel size: 2 × 2 pixels) and a sliding paraboloid
452 (radius: 5 pixels) for background subtraction. Detection of central peak positions for individual
453 NPCs was carried out with the plugin TrackMate[34], using DoG detector and adjusting the detection
454 threshold as the spot diameter size. The resulting 3D NPC coordinates were used to visualize and
455 determine flat and curved regions of the nucleus. Using this map, circular and ellipsoidal ROIs
456 could then be selected in the flatter parts containing central NPC positions within the Z-depth of
457 approx. 500 nm, which corresponds to 2–3 microscopic slices in the images. The remaining signal
458 outside the ROIs, as in curved regions or cytoplasmic structures were discarded from further
459 analysis. NPC densities were calculated for each cell separately by dividing the number of NPCs
460 within the selected ROIs by the corresponding ROI areas. For each cell line, the values were
461 combined to calculate the mean and median NPC density values.
462

463 **Quantification of Nup copy number in the cytoplasm and the nucleoplasm as well as in non-**
464 **core and core regions of the NE**

465 Mitotic cells were imaged and monitored from anaphase onset for two hours in 3D by confocal
466 microscopy. The microscopy setup and the imaging conditions are described above. Time-lapse
467 imaging for mEGFP-tagged Nups was performed every 30 sec. Photobleaching was negligible and
468 thus not corrected. Time-lapse imaging for Pom121-mCherry was carried out every 60 sec, and
469 photobleaching was corrected by measuring a fluorescence signal decay in a neighboring cell in
470 the same field of view. Visualization of the chromosome surface in 3D was done in the Amira
471 software package[35].

472 To measure the Nup accumulation on the NE, single planes were selected that contain the
473 largest nuclear area at individual time points to avoid underestimation of the signal as mentioned
474 earlier. The Nup intensity was quantified on the NE mask with the width of 0.75 μm that was
475 generated from a SiR-DNA signal at each time point. Except for Nup107 and Seh1, the Nup signal
476 in the cytoplasm and nucleoplasm was measured and used as background. For Nup107 and Seh1,
477 only the cytoplasmic signal was used as background because of their localization at kinetochores.
478 These background values were quantified at individual time points and subtracted from the Nup
479 intensities on the NE. The measured Nup intensity was converted into the concentration and then
480 multiplied with nuclear surface area to calculate the total number of the Nups on the NE. For
481 Nup153 and Pom121, we did not convert the fluorescence intensity to the concentration as the cell
482 lines were not fully validate to be homozygously-tagged.

483 The Nup copy number was also calculated in the cytoplasm and the nucleoplasm during first
484 two hours after anaphase onset. The cytoplasm mask was created by subtracting a mask of the
485 nucleus generated from a SiR-DNA signal from a mask of the whole cell generated from a
486 mEGFP-Nup signal. The mask for the nucleoplasm was created by eroding three pixels of the
487 nuclear mask generated from a SiR-DNA signal. The Nup fluorescence intensity was quantified
488 on these cytoplasmic and nucleoplasmic masks over time and then converted into the
489 concentration. To calculate the total number of Nups in the cytoplasm and the nucleoplasm, the
490 measured concentration was multiplied by the volume of the respective compartments. For the
491 cytoplasm volume, we used the value that was measured previously using fluorescently-labelled
492 dextran[22]. The nucleoplasmic volume was quantified in each mEGFP-Nup knock-in cell line using
493 a SiR-DNA signal as described previously[12].

494 Core regions were predicted on the NE based on a previously described protocol using the
495 core marker Lap-2α[12]. Briefly, nuclear volume was segmented using SiR-DNA fluorescence
496 signals that were processed with a 3D Gaussian filter and a multi-level thresholding. Nuclear

volume was then divided into inner and outer volumes using the cutting plane that was constructed from the largest eigenvector and the second one orthogonal to the first vector of the pixel coordinates of the nuclear volume. Surface area of each nucleus was calculated and utilized to adjust the size of the inner and outer core regions at individual time points. The previously defined criteria for being core and non-core regions[12] was applied. The position of inner and outer core was determined with respect to the intersection point of the largest eigenvector on the nuclear surface.

Mathematical modeling for the nuclear pore assembly kinetics

Previous EM data showed that, within 2 hours after anaphase onset, postmitotic assembly is the dominant process in the non-core region, whereas the slower interphase assembly prevails in the core region[12]. Assuming that this relation is also reflected in the live-cell Nup dynamics, we derived a mathematical model. We assumed that the observed total fluorescence intensity in the non-core, $n(t)$, and core region, $c(t)$, at time-point *t* after anaphase onset is a linear combination of the postmitotic and interphase assembly processes according to

$$n(\mathrm{t}) = \mathrm{f_N} pm(\mathrm{t}) + (1 - \mathrm{f_N}) ip(\mathrm{t}) \tag{1}$$

$$c(\mathrm{t}) = \mathrm{f_C}\, pm(\mathrm{t}) + (1 - \mathrm{f_C})\, ip(\mathrm{t}), \tag{2}$$

where $pm(t)$ and $ip(t)$ are the postmitotic and interphase assembly, respectively. The fraction of postmitotic assembly in the non-core and core regions are denoted f_n and f_c, respectively. To test this assumption and obtain an estimate of the fractions, we used a phenomenological model that accounts for the observed sigmoid-like kinetics

$$pm(t) = \frac{t^{n_p}}{t^{n_p} + K_p^{n_p}}, \qquad \text{for } t \geq d \tag{3}$$

$$ip(t) = \frac{t^{n_i}}{t^{n_i} + K_i^{n_i}}, \qquad \text{for } t \geq d \tag{4}$$

516 and $pm(t < d) = ip(t < d) = 0$. The parameters n_p, K_p and n_i, K_i characterize the postmitotic
517 and interphase kinetics, respectively. The average time-point where a Nup is recruited for the
518 interphase and postmitotic assembly is K_i and K_p, respectively. The parameter d accounts for an
519 additional delay in NPC core region assembly with respect to the non-core region due to the
520 presence of kinetochore microtubule fibers[25]. For the non-core region $d = 0$. For the core region d
521 was estimated from the data.

522 For each assembly mechanisms, we also computed the recruitment duration from Eqs. 3–4.
523 For instance, the time required to recruit 80% of the protein, i.e. from a fraction of $\alpha_1 = 0.1$ up
524 to $\alpha_2 = 0.9$, is given by (see also Extended Data Fig. 4a)

$$\Delta T_p = K_p \left(\left(\frac{\alpha_2}{1-\alpha_2} \right)^{\frac{1}{n_p}} - \left(\frac{\alpha_1}{1-\alpha_1} \right)^{\frac{1}{n_p}} \right) \tag{5}$$

$$\Delta T_i = K_i \left(\left(\frac{\alpha_2}{1-\alpha_2} \right)^{\frac{1}{n_i}} - \left(\frac{\alpha_1}{1-\alpha_1} \right)^{\frac{1}{n_i}} \right). \tag{6}$$

525 In the model, we subtracted a background computed from the average of the first 3 time points.
526 All data is subsequently normalized to the mean value between 100 and 120 min after anaphase
527 onset. This yields corrected fluorescence intensities, $N(t_j)$ and $C(t_j)$. To find the model
528 parameters we minimized the mean squared distance between data and model for all the time
529 points M

$$\chi^2 = \sum_{j=1}^{M} \left(\left(\frac{N(t_j) - n(t_j)}{\sigma_N(t_j)} \right)^2 + \left(\frac{C(t_j) - c(t_j)}{\sigma_C(t_j)} \right)^2 \right), \tag{7}$$

530 where $\sigma_N(t_j)$ and $\sigma_C(t_j)$ are the respective standard deviation in the non-core and core region.

531 The parameter estimation has been performed in two steps. First, for each protein/cell-line,
532 we estimated the postmitotic fraction in the core and non-core region and the kinetic parameters.
533 All in all we computed 60 parameters (6 parameters per protein) from 4446 data points. We found
534 that the model well agrees with the data (Extended Data Figs. 2 and 3, $R^2 > 0.99$). For the

535 postmitotic fractions, we obtained on average f_n = 0.857 [0.76, 0.95] and f_c = 0.295 [0.17, 0.4],
536 where the number in brackets indicates the 95% confidence interval as estimated using the profile
537 likelihood method[36]. Importantly, the obtained postmitotic fractions are well in agreement with
538 the previously reported estimates obtained from EM-data[12]. The delay in pore formation between
539 core and non-core region was estimated by systematically varying d from 0 to 6 min in steps of 1
540 minute. A value of d = 2 min, gave optimal result. In a second step we used the previously
541 estimated average postmitotic fractions and d and recomputed the kinetics parameters for each
542 protein. The model with reduced parameters gave very similar results. To verify if the choice of
543 common postmitotic fractions for all Nups is valid, we computed the Baysian information criterion
544 (BIC) according to the previous report[37]. The difference in BIC between the model with reduced
545 parameters, 42 parameters for all proteins, compared to the full model, 60 parameters, was -7,
546 indicating that the model with reduced parameters is justified. The obtained parameter values are
547 listed in Extended Data Table 2.

548 Our validated model can be used to derive the underlying post-mitotic and interphase
549 assembly kinetics. Using Eqs. 1–2 we obtain

$$ip(t) = \frac{f_n c(t) - f_c n(t)}{f_n - f_c}. \tag{8}$$

$$pm(t) = \frac{(1 - f_c)n(t) - (1 - f_n)c(t)}{f_n - f_c}. \tag{9}$$

550 These equations can directly be applied to the experimental data N(t) and C(t) using the previously
551 estimated fraction f_n and f_c.

552 In Fig. 3c we see a strong positive correlation for the average time point of assembly and the
553 duration of assembly. One can prove that such a relation is expected for an irreversible sequential
554 assembly mechanism with linear rate constants. Using the definition for average time and
555 duration[38], the average time-point of a protein binding at step i is

$$\tau_i = \sum_{j=1}^{i} 1/k_j, \tag{10}$$

556 where k_j is the binding rate constant of a protein binding at step j to the complex. The duration of
557 assembly of a protein binding at step i is given by

$$\theta_i = 2\sqrt{\sum_{j=1}^{i} 1/k_j^2}. \tag{11}$$

558 From Eqs 10–11, it is clear that $\tau_{i+1} > \tau_i$ and $\theta_{i+1} > \theta_i$ for any parameter combinations.
559 Therefore, late binding proteins show a longer duration of assembly.
560

561 **Structural modeling of NPC assembly pathway**

562 A model of the assembly pathway is defined by a series of static structures, including a static
563 structure at each sampled time point along the assembly process. Therefore, we model the NPC
564 assembly by first modeling static structures at each time point, independently from each other. We
565 then enumerate alternative assembly pathways and rank them based on the static structure scores
566 and plausibility of transitions between successive static structures.

567 *Integrative modeling of static structures at each time point*

568 The static structures are modeled by standard integrative structure modeling[29], as follows.

569 *Representing a static structure model*

570 The time points correspond to times with available ET protein densities[11]: 5min, 6 min, 8 min, 10
571 mins, and 15 min after anaphase onset. We divide the mature NPC structure (PDB 5a9q, 5ijo) into
572 eight spokes and further divide each spoke into a set of rigid subcomplexes, including the Y-
573 complex, the inner ring Nup205-Nup155-Nup93 subcomplex, the inner ring Nup93-Nup188-
574 Nup155 subcomplex, and the central channel Nup62-Nup58-Nup54 subcomplex. For each
575 domain, we coarse-grained the structure by grouping 10 consecutive amino acid residues into a
576 single bead at the center of mass of those residues. Each subcomplex is represented as a rigid body.

577 The NE is represented as a fixed toroid surface embedded in two parallel planes. Thus, the
578 variables of the model include the Euclidean coordinates of the Nup subcomplexes and the copy
579 number of each Nup subcomplex.

580 We set the inner pore diameter and minor radius of the pore at each time point to the mean of
581 previously determined NE cross sections[11] with a pore diameter of 51.5 nm, 58.4 nm, 72.7 nm,
582 84.6 nm, 79.8 nm, and 87 nm; and minor radius of 21.4 nm, 21.2 nm, 21.5, 20.3 nm, 17.1 nm and
583 15 nm for time points at 5min, 6min, 8min, 10min, 15min, and the mature pore, respectively.

584 *Scoring a static structure model*

585 The copy numbers of the NPC subcomplexes at each time point were restrained by a Gaussian
586 function with mean and variance determined by the single-cell traces presented in this study. The
587 relative likelihood of a set of copy numbers is proportional to the product of individual Gaussian
588 likelihoods.

589 Distances between pairs of Nups that are in contact with each other in the native NPC
590 structure[26,27] were restrained by a harmonic Gō-like model[39]. Inter-subcomplex contacts within 5
591 nm in the mature structure were restrained by a harmonic function (strength 0.01 kcal/mol Å).
592 Each Gō-like scoring term was scaled at each time point, from zero at the first time point to full
593 strength at the mature pore time point. Distances between all pairs of Nups were also restrained
594 by a harmonic excluded volume restraint (strength 0.01 kcal/mol Å). Proximity between Nup
595 domains containing a membrane interacting ALPS-motif and the NE was restrained by a harmonic
596 term (strength 0.1 kcal/mol Å), based on their sequences. Overlap between the Nups and NE
597 surface was avoided by imposing a harmonic repulsion between the Nups and NE surface (strength
598 of 0.01 kcal/mol Å).

599 The shape of a static structure was restrained by a correlation coefficient between the model
600 and ET protein density[11]. The forward model density was represented by fitting each Nup
601 subcomplex with a Gaussian mixture model of two components per subcomplex copy using the

602 *gmconvert* utility[40]. Similarly, the ET protein densities at each time point were represented with a
603 Gaussian mixture model with 150 components fit to the experimental density.

604 *Sampling static structure models*

605 A state of the NPC at any given time point is defined by the copy numbers and coordinates of its
606 components. Only copy number assignments and structures consistent with the C-8 symmetries
607 were sampled. In addition, we only sampled structures for the top 20-scoring Nup copy number
608 combinations. Each sampling started with the mature pore structure, followed by applying 10^6
609 Monte Carlo moves. These moves included rotational and translational perturbations to each Nup
610 subcomplex, drawn from a uniform distribution in the range from -0.04 to +0.04 radians and from
611 -4 to +4 Å, respectively.

612 *Modeling the assembly pathway*

613 With the static structure models in hand, we connect them into complete alternative assembly
614 pathways, as follows.

615 Each pathway is represented by a static structure at each sampled time point, starting with t =
616 5 min and culminating in the native structure; we do not model the completely disassembled NPC.
617 The score of a pathway is the sum of the scores for the static structures on the pathway (defined
618 above) and transitions between them. A transition score is uniform for all allowed transitions. A
619 transition between two successive static structures is allowed if the subcomplexes in the first
620 structure are included in the second structure. All possible pathways were enumerated, scored, and
621 ranked. The best-scoring pathways were extracted for further analysis (Fig. 4).

622

623 **Sample size determination and statistical analysis**

624 For quantitative imaging in Fig. 1a, d, the data were from 4, 4, 4, 2, 3, 2, 3, and 2 independent
625 experiments for Nup107, Seh1, Nup205, Nup93, Nup62, Nup214, Tpr and Nup358, respectively.
626 STED imaging in Fig. 1b, c was from one independent experiment. For dynamic quantitative

627 imaging in Fig. 2, the data were from 4, 4, 4, 2, 3, 4, 3, 2, 2, and 4 independent experiments for
628 Nup107, Seh1, Nup205, Nup93, Nup62, Nup214, Tpr, Nup358, Nup153, and Pom121,
629 respectively. Statistical analyses were performed only after all the data were taken. Sample sizes
630 for each experiment are indicated in figure legends. Sample sizes were based on pilot experiments
631 to determine the number of cells required to observe stable population averages with high
632 Pearson's correlation between replicates. Videos of dividing cells with rotating nuclei are removed
633 from the analysis, because we cannot properly assign the non-core and core regions.
634

635 **Data and code availability**

636 Fluorescence images will be available in the Image Data Resource (IDR;
637 https://idr.openmicroscopy.org/) or the BioImage Archive
638 (https://www.ebi.ac.uk/biostudies/BioImages/studies). Our integrative spatiotemporal model of
639 the postmitotic assembly of the human NPC is available in PDB-Dev (https://pdb-
640 dev.wwpdb.org/) under the accession code XX (PDB submission in progress). Integrative
641 Modeling Platform (IMP) is an open source program freely available under the LGPL license at
642 http://integrativemodeling.org; all input files, scripts, and output files are available at
643 http://integrativemodeling.org/npcassembly.
644

645 **Method references**

646 32 Landry, J. J. *et al.* The genomic and transcriptomic landscape of a HeLa cell line. *G3*
647 *(Bethesda)* **3**, 1213–1224 (2013).
648 33 Farrants, H. *et al.* Chemogenetic Control of Nanobodies. *Nat. Methods* **17**, 279–282
649 (2020).
650 34 Tinevez, J. Y. *et al.* TrackMate: An open and extensible platform for single-particle
651 tracking. *Methods* **115**, 80–90 (2017).

652 35 Pruggnaller, S., Mayr, M. & Frangakis, A. S. A visualization and segmentation toolbox for
653 electron microscopy. *J. Struct. Biol.* **164**, 161–165 (2008).
654 36 Raue, A. *et al.* Structural and practical identifiability analysis of partially observed
655 dynamical models by exploiting the profile likelihood. *Bioinformatics* **25**, 1923–1929
656 (2009).
657 37 Kass, R.E. & Raftery, A. E. Bayes Factors. *J. Am. Stat. Assoc.* **90**, 773–795 (1995).
658 38 Heinrich, R., Neel, B. G., & Rapoport, T. A. Mathematical models of protein kinase signal
659 transduction. *Mol. Cell* **9**, 957-70 (2002).
660 39 Go, N. & Abe, H. Noninteracting local-structure model of folding and unfolding transition
661 in globular proteins. I. Formulation. *Biopolymers* **20**, 991–1011 (1981).
662 40 Kawabata, T. Gaussian-input Gaussian mixture model for representing density maps and
663 atomic models. *J. Struct. Biol.* **203**, 1–16 (2018).
664

665 **Acknowledgments**

666 We thank the EMBL Advanced Light Microscopy Facility (ALMF) for their support in STED
667 super-resolution microscopy; Ben Webb for help with IMP and Josh Baker-Lepain for managing
668 the Wynton computer cluster at QBI@UCSF. This work was supported by grants from the Baden
669 Wuerttemberg Foundation (J.E. and A.S.), NIH/NIGMS R01GM083960 (A.S.), NIH/NIGMS
670 P41GM109824 (A.S.), NIH/NIGMS R01GM112108 (A.S.) and the European Molecular Biology
671 Laboratory (EMBL; S.O., A.Z.P., A.R., M.J.H., M.K., A.C., B.K., J.E.). S.O. and A.R. were
672 further supported by the EMBL Interdisciplinary Postdoc Programme (EIPOD) under Marie Curie
673 Actions COFUND. S.O. was additionally supported by a JSPS fellowship (The Japan Society for
674 the Promotion of Science, postdoctoral fellowship for research abroad).
675

676 **Author contributions**

677 SO, JOBT, AS, and JE designed the project. SO performed all the fluorescence microscopy
678 experiments and analyses. JOBT performed integrated structural modeling. AZP carried out
679 mathematical modeling for the nuclear pore assembly kinetics. AR developed an analysis pipeline
680 for nuclear pore density measurement. MJH established a computational image analysis pipeline
681 to quantify fluorescence intensities in non-core and core regions in 3D time-lapse images. M.K.,
682 A.C. and B.K. generated genome-edited cell lines. AS and JE supervised the work. SO, JOBT,
683 AS, and JE wrote the paper. All authors contributed to the analysis and interpretation of data and
684 provided input on the manuscript.
685
686 **Competing interest declaration**
687 The authors declare no competing interests.
688
689 **Additional information**
690 The manuscript contains supplementary material (Extended Data Figs. 1 to 4 and Extended Data
691 Tables 1 to 3).